JCI The Journal of Clinical Investigation

An inducible RIPK3-driven necroptotic system enhances cancer cell-based immunotherapy and ensures safety

Kok-Siong Chen, … , Natalia Claire Mendonca, Khalid Shah

J Clin Invest. 2024. https://doi.org/10.1172/JCI181143.

Research In-Press Preview **Immunology** **Oncology**

Recent progress in cancer cell-based therapies has led to effective targeting and robust immune responses against cancer. However, the inherent safety risks of using live cancer cells necessitate the creation of an optimized safety switch without hindering the efficacy of immunotherapy. The existing safety switches typically induce tolerogenic cell death, potentially leading to an immunosuppressive tumor immune microenvironment (TIME), which is counterproductive to the goals of immunotherapy. Here, we developed and characterized an inducible RIPK3-driven necroptotic system that serves as a dual function of safety switch as well as inducing immunogenic cell death which in turn stimulates antitumor immune responses. We showed that activating RIPK3 safety switch triggered immunogenic responses marked by an increased release of adenosine triphosphate (ATP) and damage-associated molecular patterns (DAMPs). Compared to other existing safety switches, incorporating RIPK3 system inhibited tumor growth, improved survival outcomes in tumor-bearing mice, and fostered long-term antitumor immunity. Moreover, RIPK3 system reinvigorated the TIME by promoting dendritic cell (DC) maturation, polarizing the macrophages towards the M1 phenotype, and reducing the exhaustion of $CD4^+$ and $CD8^+$ T lymphocytes. Our study highlights the dual role of RIPK3-driven necroptotic system in improving the safety and efficacy of cancer cell-based therapy, with broader implications for cellular therapies.

An inducible RIPK3-driven necroptotic system enhances cancer cell-based immunotherapy and ensures safety

Kok-Siong Chen[1,2], Sarah Manoury-Battais[1,2,3], Nobuhiko Kanaya[1,2], Ioulia Vogiatzi[1,2], Paulo Borges[1,2], Sterre Kruize[1,2], Yi-Ching Chen[1,2], Laura Y Lin[1,2], Filippo Rossignoli[1,2], Natalia Claire Mendonca[1,2], and Khalid Shah[1,2,4]*

[1]Center for Stem Cell and Translational Immunotherapy, Brigham and Women's Hospital, Harvard Medical School, Boston, MA 02115

[2]Department of Neurosurgery, Brigham and Women's Hospital, Harvard Medical School, Boston, MA 02115

[3]Department of Education and Research in Biology, ENS Paris-Saclay, Université Paris-Saclay, Gif-sur-Yvette 91190

[4]Harvard Stem Cell Institute, Harvard University, Cambridge, MA 02138

*Corresponding author:

Khalid Shah, kshah@bwh.harvard.edu; 857-307-5233; 60 Fenwood Road, Brigham and Women's Hospital, Boston, MA 02115

Abstract:

Recent progress in cancer cell-based therapies has led to effective targeting and robust immune responses against cancer. However, the inherent safety risks of using live cancer cells necessitate the creation of an optimized safety switch without hindering the efficacy of immunotherapy. The existing safety switches typically induce tolerogenic cell death, potentially leading to an immunosuppressive tumor immune microenvironment (TIME), which is counterproductive to the goals of immunotherapy. Here, we developed and characterized an inducible RIPK3-driven necroptotic system that serves as a dual function of safety switch as well as inducing immunogenic cell death which in turn stimulates antitumor immune responses. We showed that activating RIPK3 safety switch triggered immunogenic responses marked by an increased release of adenosine triphosphate (ATP) and damage-associated molecular patterns (DAMPs). Compared to other existing safety switches, incorporating RIPK3 system inhibited tumor growth, improved survival outcomes in tumor-bearing mice, and fostered long-term antitumor immunity. Moreover, RIPK3 system reinvigorated the TIME by promoting dendritic cell (DC) maturation, polarizing the macrophages towards the M1 phenotype, and reducing the exhaustion of CD4+ and CD8+ T lymphocytes. Our study highlights the dual role of RIPK3-driven necroptotic system in improving the safety and efficacy of cancer cell-based therapy, with broader implications for cellular therapies.

Introduction:

Therapeutic tumor cells hold promise as anticancer agents due to their ability to serve as the natural source of neoantigens and the ease of being genetically engineered. We recently developed cancer cell-based therapies using live tumor cells that not only target tumor cells directly but also potentiate the immune system's response, leading to immune-mediated cell death(1). To heighten the safety of this therapeutic approach, it is necessary to incorporate suicide systems/kill switches. The commonly used safety switches, herpes simplex virus thymidine kinase (HSV-TK)(2), inducible caspase 9 (iCasp9)(3), and CD20/rituximab system(4), typically induce a tolerogenic form of cell death which may lead to an immunosuppressive tumor microenvironment(5). These attributes of existing safety switches inadvertently oppose the goals of immunotherapy by dampening the desired immune response against cancer cells. Given these limitations, there is an urgent need to explore better approaches to suicide systems.

One such approach is the inducible immunogenic cell death (ICD) suicide system. Characterized by the exposure of damage-associated molecular patterns (DAMPs) and a cascade of intracellular events leading to robust anti-tumor immunity(6-8), ICD distinguishes itself from other types of cell death with its capacity to stimulate a potent immune response against tumor cells. Unlike apoptosis, a non-inflammatory form of cell death, necroptosis is a programmed cell death that leads to the release of DAMPs which can stimulate an immune response(9-13). Specifically, necroptosis occurs downstream of the receptor-interacting protein kinase-1 and 3 (RIPK1 and RIPK3)(14). These proteins oligomerize through their RIP homotypic interaction motif (RHIM) to form the necrosome together with mixed lineage kinase domain-like protein (MLKL), thereby inducing necroptosis(14). Throughout the whole process, RIPK3 homodimerization and phosphorylation are the key events triggering the immunogenic cell death of necroptosis(15). Leveraging this phenomenon in the context of a suicide system could therefore provide dual benefits– safety control and potential therapeutic augmentation.

Recognizing the specific need for a dual system that allows immunogenic cell killing and a reliable kill switch in cancer cell-based immunotherapies, we developed and evaluated an inducible RIPK3-driven necroptotic suicide system using whole tumor cancer cell vaccine as therapeutics to treat glioblastoma (GBM). We first devised the switch by optimizing previously published designs of RIPK3 dimerization constructs(16, 17), which were utilized to study the necroptotic pathway. Our aim was to ensure that the necroptotic suicide mechanism is independent of RIPK1 dimerization, thereby avoiding Caspase-8 negative regulation. This design allows for the conditional dimerization and activation of the RIPK3 protein upon exposure to a synthetic dimerizing drug. Next, we tested the activity of the safety switch by introducing the gene into GBM tumor cells and further evaluated the immunogenicity induced by the cell death, both *in vitro* and *in vivo*, in comparison to existing safety switches. Our goal was to evaluate the unique *in vivo* immune responses elicited by this approach in combination with cancer cell-based therapy. Our findings reveal that RIPK3-driven necroptotic suicide system has an immense potential to combine safety with enhanced therapeutic impact via improving anti-tumor immune responses.

Results:

Robust necroptotic signaling correlates with improved therapeutic outcomes for cancer patients

To understand how the necroptotic signaling within the tumor microenvironment (TME) affects the patients' clinical outcome, primary tumor samples in TCGA dataset were co-clustered based on both Gene Ontology apoptotic (GO:0097190) and necroptotic (GO:0097527) signaling pathway gene signatures, and 4 clusters were generated (Fig. 1A and table S1). Based on the combined gene score (upregulation of necroptotic signaling and downregulation of apoptotic signaling) for each cluster, C2 was associated with the most robust necroptotic signaling ($Necroptosis^{Hi}$) and low apoptotic signaling ($Apoptosis^{Low}$), whereas C1 had the least score for necroptotic signaling ($Necroptosis^{Low}$) but highest apoptotic signaling ($Apoptosis^{Hi}$) (Fig. 1A and table S1). Importantly, $Necroptosis^{Hi}Apoptosis^{Low}$ as reflected by the C2 was associated with an improved clinical outcome and a significantly better prognosis compared to C1 which is $Apoptosis^{Hi}$ $Necroptosis^{Low}$ (Fig. 1B and table S1). We also confirmed that C2 samples have a significantly higher expression of high-mobility group box 1 (HMGB1), a typical DAMP that is released during necroptosis(18) (Fig. 1C). A similar analysis (Fig. 1D and table S2) using CCGA glioma patients mRNAseq public dataset (19) demonstrated that C3 ($Necroptosis^{Hi}Apoptosis^{Low}$) is associated with a better survival probability compared to C2 ($Apoptosis^{Hi}$ $Necroptosis^{Low}$) (Fig. 1E and table S2), but no significant difference of HMGB1 expression was observed (Fig. 1F). These findings suggest that upregulation of necroptotic signaling and downregulation of apoptotic signaling within the TME is likely to improve clinical outcome for patients, highlighting the association of necroptotic signaling in shaping a more immune active TME.

Generation of engineered tumor cells with an inducible RIPK3-driven necroptotic safety switch

To establish an inducible RIPK3-driven necroptotic suicide system, a murine RIPK3 cDNA fragment encoding $FKBP^{F36V}$ and mutated RHIM domains were cloned into a third-generation lentiviral transfer vector based on previously published RIPK3 dimerization constructs(16, 17) (Fig. 1G). For enhanced

specificity, we opted to use a mutated form of FKBP rather than the wild-type protein(20). The cDNA fragment for $FKBP^{F36V}$ domain was fused to the N-terminal of RIPK3 to allow autophosphorylation and activation of RIPK3 protein upon homodimerization(16, 17), thus activating necroptosis. The RHIM domain was mutated to prevent the interaction of RIPK3 with endogenous RIPK1, thereby avoiding RHIM-dependent necrosome formation and subsequent regulation by caspase-8 (16, 17). This system allows the inducible intracellular homodimerization of RIPK3 proteins upon administration of AP20187 (B/B homodimerizer, hereinafter referred to as "B/B"), a rapamycin analog.

To test the safety switch *in vitro*, we transduced CT2A, an immune-suppressive syngeneic GBM cell line (21) with the RIPK3 lentiviral construct resulting in the engineered CT2A line (hereinafter referred to as "CT2A-RIPK3"). Compared to wildtype CT2A, the viability of CT2A-RIPK3 cells reduced upon the B/B treatment in dose-dependent and time-dependent manners (Fig. 1H). Moreover, Western Blot analysis on cell lysates of B/B treated CT2A-RIPK3 showed the phosphorylation of MLKL and RIPK3 but no cleaved-Caspase3 expression (Fig. 1I, Fig. S4), confirming the activation of necroptotic signaling and the cell death observed was not apoptotic-driven. To validate the inducible suicide system of the engineered tumor cells *in vivo*, CT2A and CT2A-RIPK3 tumor cells were implanted intracranially in immunocompetent C57BL6 mice (Fig. 1J). Bioluminescent Fluc imaging (BLI) revealed aggressive tumor growth for all mice implanted with CT2A and CT2A-RIPK3 (Fig. 1K). Upon intraperitoneal administration of B/B, a complete tumor eradication was observed in CT2A-RIPK3-bearing mice (Fig. 1K). Furthermore, the tumor-free mice survived until the termination of the experiment (Fig. 1L), confirming the effectiveness of the inducible RIPK3 safety switch on tumor cells *in vivo*.

Cell death induced by RIPK3 safety switch is more immunogenic than RapaCas9 and HSV-TK systems *in vitro*

Recently, we have developed a two-layered safety switch that comprises RapaCas9 and HSV-TK suicide systems for safer cell therapies (22). Although these systems have been tested extensively *in vitro* and *in*

vivo (1, 22), the immunogenicity induced by cell death has not been investigated yet. Given the release of adenosine triphosphate (ATP) from dying cells and the postmortem release of HMGB1 into the extracellular space are two of the three major hallmarks of ICD(23), we sought to compare the cell death immunogenicity of these three safety switches based on these two measures. As such, we engineered CT2A to express RapaCas9TK using the LV-RapaCas9TK construct (22) (hereinafter referred to as "CT2A-RC9TK"). For a fair comparison between these three safety switches, we first determined their half-maximal effective concentration (EC_{50}) with different doses of the drugs and the durations of the treatment. The EC_{50} for B/B to induce cell death in CT2A-RIPK3 was 1nM (Fig. 1H) post 5 hours of treatment (Fig. 2A). To induce cell death in CT2A-RC9TK, the EC_{50} for rapamycin (RapaCas9 system) was 25nM (Fig. 2B) post 9 hours of treatment (Fig. 2C) and ganciclovir (HSV-TK system) was 0.1μg/mL (Fig. 2D) post 72 hours of treatment (Fig. 2E). Western Blot analysis for the cell lysate of CT2A-RIPK3 treated with B/B showed phosphorylation of MLKL and RIPK3 but not in CT2A-RC9TK treated with rapamycin or GCV respectively (Fig. 2F). On the other hand, the expression of cleaved-Caspase3 was observed in the cell lysates of CT2A-RC9TK treated with GCV or rapamycin but not in other groups (Fig. 2F, Fig. S5), confirming the induction of caspase-dependent apoptosis. Next, we confirmed HMGB1 expression in the supernatant for B/B-treated CT2A-RIPK3 and GCV/rapamycin-treated CT2A-RC9TK (Fig. 2F). Furthermore, the highest fold change of the ATP release relative to control was observed in supernatant collected at EC50 for B/B-treated CT2A-RIPK3 compared to the other two suicide systems (Fig. 2G). These findings reveal that cell death induced by RIPK3 safety switch is necroptotic and more immunogenic.

Tumor cell death induced by RIPK3 safety switch elicits a long-term immunity *in vivo*

To investigate the cell death immunogenicity for each safety switch *in vivo*, intracranial implantation of CT2A-RIPK3 and CT2A-RC9TK was performed in immunocompetent C57BL6 mice (Fig. 3A). The intracranial tumors of 4 out of 5 CT2A-RIPK3 bearing mice were completely eradicated upon the B/B treatment at day 7 post tumor implantation (Fig. 3B). These mice remained tumor-free and survived beyond

30 days (Fig. 3C). For CT2A-RC9TK, 4 out of 5 tumor-bearing mice treated with GCV at day 7 post tumor implantation had complete tumor eradication (Fig. 3D) and these mice remained tumor-free and survived beyond 30 days (Fig. 3E). For CT2A-RC9TK tumor-bearing mice treated with rapamycin, 3 out of 5 of them had complete tumor eradication (Fig. 3D) and these mice also remained tumor-free and survived beyond 30 days (Fig. 3E). To test the immunization effects of these suicide systems, we next re-challenged the mice surviving from the first implantation at day 35 post tumor implantation with the parental CT2A cells in the contralateral brain hemisphere (Fig. 3A). The median survival for the mice from both RapaCas9 and HSV-TK groups was 15 days post re-challenge, whereas all mice from RIPK3 system group survived until the termination of the experiment and no tumor growth was observed (Fig. 3F). These findings indicate that tumor cell death induced by RIPK3 safety switch can elicit long-term antitumor immunity in mice.

Cell death induced by RIPK3 safety switch inhibits the tumor growth of the parental CT2A cells and improves survival outcomes by reinvigorating tumor immune microenvironment *in vivo*

To determine whether the cell death induced by RIPK3 suicide system has potential therapeutic augmentation, we co-implanted wildtype CT2A cells and CT2A-RIPK3 cells intracranially in C57BL6 mice (Fig. 4A). The tumor growth of the parental CT2A cells was inhibited upon the activation of RIPK3 suicide system compared to the controls (Fig. 4B). Moreover, these mice also had a significantly better survival outcome compared to the controls (Fig. 4C). These findings imply that the application of RIPK3 safety switch has antitumor therapeutic benefits.

To assess the impact of RIPK3 system on the TIME, we analyzed the immune profile (Fig. S1) after activation of the safety switch *in vivo* (Fig. 4A). Control groups were used to ensure observed changes were due to induced cell death and not just the presence of different cell types or the drug. Overall, we observed reduced T cells in the TME (Fig. 4D). Although the relative number of DC remained unchanged (Fig. 4D), the number of DC2 and mature DCs significantly increased (Fig. 4E), suggesting that the cell death induced by RIPK3 safety switch promotes DC maturation and DC2-mediated immune responses. In addition, an

increased polarization of macrophages towards M1 phenotype was observed (Fig. 4F), implying an increased inflammatory factor within the TIME. For T lymphocytes, a significant reduction of exhausted CD4 (Fig. 4G) and CD8 (Fig. 4H) lymphocytes, as well as activated CD8 lymphocytes (Fig. 4H), was observed. These findings indicate a more immune-reactive environment post-RIPK3 safety switch activation.

To provide insights into potential differences in immune responses between safety switches, we also analyzed the immune profile on the TIME after activation of RapaCas9 or HSV-TK. Unlike RIPK3, activation of RapaCas9 and HSV-TK did not change the overall immune cell population (Fig. S2A) and the subpopulations of DC, macrophages, and CD4 lymphocytes (Fig. S2B-D), but a significant reduction of exhausted, effector, or activated CD8 lymphocytes was observed for RapaCas9 activation (Fig. S2E).

Considering the importance of tumor-draining lymph node (TDLN) for antitumor immune responses (24), we assessed the impact of RIPK3 safety switch activation on the TDLN. We observed an increase in DC and NK cells (Fig. S3A), and a significant reduction in the DC2 (Fig. S3B). Yet, no significant changes in CD4 (Fig. S3C) and CD8 (Fig. S3D) lymphocytes were observed. These findings corroborate that cell death induced by RIPK3 safety switch reinvigorates the tumor immune environment and induces a more robust immune response than the other two systems.

RIPK3 safety switch synergistically enhances the therapeutic efficiency of cancer cell-based immunotherapy and promotes long-term immunity

To assess the synergistic therapeutic impact of the RIPK3 system and cancer cell-based therapy using live tumor cells, we sought to integrate this kill switch into the therapeutic tumor cells for treating established GBM tumors. The therapeutic tumor cells were derived from CT2A cells and genetically edited using CRISPR/Cas9 to knock out IFNAR1 and engineered to express interferon-beta (IFNβ) (1). These modified cells, referred to as cCT2A-IFNβ, were shown not to grow in mice, as evidenced in our previous research (1). Further, we engineered these cCT2A-IFNβ cells to include the RIPK3 safety switch, creating a new

cell line named cCT2A-IFNβ-RIPK3. We treated established intracranial GBM tumors in mice intratumorally with cCT2A-IFNβ-RIPK3, with or without B/B activation of RIPK3 safety switch (Fig. 5A). Activation of the kill switch significantly improved survival, completely eradicating wildtype tumors in 3 of 5 mice, in contrast to the non-activated group where all mice succumbed (Fig. 5B, C). To investigate long-term immunity, surviving mice were re-challenged with wildtype CT2A cells implanted in the contralateral hemisphere of their brains, using naïve mice as controls. Remarkably, no tumor growth was observed in the re-challenged mice (Fig. 5D), and they survived this second challenge (Fig. 5E). These results suggest that the RIPK3 system, when combined with cancer cell-based therapy, not only functions as a safety switch but also has a synergistic therapeutic effect as well as contributing to the development of adaptive immunity in mice.

To further validate the robustness and broad spectrum applicability of RIPK3 system and cancer cell-based therapy, we investigated another GBM tumor model, GL261. Similar to the CT2A model, Gl261 cells were genetically edited using CRISPR/Cas9 to knock out IFNAR1 and engineered express IFNβ and RIPK3 safety switch, creating the cGL261-IFNβ-RIPK3 cell line. These modified cells were used to treat established GL261 tumors in mice. Consistent with the results from the CT2A model, activation of the RIPK3 safety switch in the cGL261-IFNβ-RIPK3 treated mice significantly improved survival (Fig. 5F, G) and the fully treated mice survived the second challenge (Fig. 5H, I). The results from both tumor models support the conclusion that the RIPK3-driven necroptotic safety switch enhances the therapeutic efficacy of cancer cell-based therapies and promotes long-term immunity across different tumor models, thereby reinforcing the potential clinical applicability of this approach.

Discussion

In this study, we repurposed and characterized a dual-function inducible RIPK3-driven necroptotic suicide system that functions as a safety switch and can synergistically boost the efficiency of cancer cell-based immunotherapy which in turn induces long-term immunity that prevents recurrence. Our findings revealed the potential of necroptotic signaling in shaping a more immune-active TIME, with the RIPK3 system showing a marked increase in ATP and HMGB1 release, indicating its heightened immunogenicity due to the induced cell death. Furthermore, the RIPK3 system demonstrated the ability to stimulate prolonged antitumor immunity in mice, inhibit tumor growth, and enhance survival outcomes.

Previous studies have shown that the introduction of ectopic necroptotic cells into the tumor milieu induces an anti-tumor response (13), but the design of the RIPK3 construct used may permit negative regulation by RIPK1 and caspase-8 which is undesirable in a safety switch context due to the risk of attenuating the necroptotic signal. Our studies extend these findings by addressing the safety concerns inherent in using live cancer cells for therapy. Our study not only reaffirms the beneficial role of RIPK3 axis in initiating tumor immunity but also innovates upon it by presenting a dual-function necroptotic switch that mitigates the safety risks and elevates the immunotherapeutic potential of cancer cell-based therapies, providing a compelling case for clinical exploration.

In recent years, efforts have been made to repurpose tumor cells as carriers for delivering anticancer agents directly to primary tumor sites. Prominent strategies include employing tumor cells as vehicles for oncolytic viruses(25, 26) and engineering them to secrete therapeutic agents targeting the tumor's neovascular endothelium(27, 28). Typically, these cells are inactivated through lysis or irradiation before reintroduction into the body. This approach has been shown to trigger robust immune cell trafficking to the tumor site (29-32), resulting in the induction of an antitumor immune response in different cancer types in pre-clinical studies (33-37). Yet, clinical benefits in Phase I-III clinical trials have been limited(38-40), likely due to the lack of active tumor targeting ability of the lysed cells. Unlike inactivated tumor cells, living tumor cells

inherently possess the ability to home in on and target tumor sites, making the use of engineered living tumor cells as therapeutics a logical step forward(1, 41). However, the safety concerns associated with this approach remain a major barrier to clinical translation. Therefore, the integration of an effective kill switch that does not compromise therapeutic efficacy is crucial. Our data suggest that the dual-function RIPK3-driven necroptotic safety switch offers a promising avenue to address the safety concerns associated with these therapies as well as synergistically enhance the therapeutic efficacy. The rationale behind introducing the tumor cells expressing IFNβ in our study (Fig. 5) was to specifically assess the synergistic therapeutic impact when combined with the RIPK3 safety switch. Our earlier experiments (Fig. 4) demonstrated therapeutic effects using CT2A cells without IFNβ modification, confirming that the RIPK3 safety switch functions independently of IFNβ signaling. The CT2A-IFNβ system allowed us to explore potential synergy without implying a dependence on IFNβ for the RIPK3 switch's function, thereby reinforcing the versatility and robustness of our approach.

The necroptotic-based safety switch offers several advantages. The type of cell death induced by the safety switch plays a pivotal role in shaping the TIME(5). Unlike apoptosis, which is relatively less inflammatory(42), necroptosis resulted in the release of DAMPs and ATP (Fig. 2G and H), signifying the immunogenic nature of this type of cell death. The results from our TCGA dataset analysis further validated the importance of necroptotic signaling in improving clinical outcomes for cancer patients. This underscores the potential of necroptosis in shaping a more immune-active TIME, which is critical for the success of immunotherapies(43).

In our in vitro and in vivo experiments, we observed that the engineered CT2A-RIPK3 cells, upon treatment with the synthetic dimerizing drug B/B, underwent necroptosis, thereby validating the functionality of this safety switch. The effectiveness of this system was further confirmed in vivo, where we observed complete tumor eradication in mice. Moreover, our study highlights the immunogenic nature of cell death induced by the RIPK3 system compared to other safety switches like RapaCas9 and HSV-TK. This is an important

finding, as it demonstrates the potential of the RIPK3 system to not only act as a safety switch but also to contribute to inducing stronger immune responses for immunotherapy.

The ability of the RIPK3-driven safety switch to induce long-term immunity, as evidenced by our findings, marks a meaningful stride in cancer immunotherapy, especially in the context of tumor recurrence prevention. The observed changes in DC populations and T lymphocyte behavior post-RIPK3 activation are particularly telling. The significant increase in mature DC (Fig. 4E), underscores a shift towards an environment conducive to enhanced antigen presentation as mature DCs are more effective in presenting tumor antigens(44, 45), leading to a more potent and targeted immune response. We observed a diminished infiltration of total T cells (Fig. 4D) following the activation of the RIPK3 safety switch, which can be explained by the significant reduction in exhausted CD4+ and CD8+ T cell population (Fig. 4G and 4H), a subset characterized by impaired function and reduced anti-tumor activity. Despite the limitations of our flow cytometry panel that included only PD-1 as a marker of exhaustion, the substantial reduction in PD-1+ cells suggests an overall shift towards a less exhausted, more functionally competent T cell phenotype. Additionally, the remaining CD8+ T cells, despite being fewer, may exhibit superior functionality due to reduced exhaustion and improved antigen presentation by mature DCs. This is further supported by the unchanged number of cytotoxic CD8+ T cells in the TME, which are crucial for tumor killing. Moreover, the increased polarization of macrophages towards M1 phenotype in the TME following RIPK3 activation (Fig. 4F) suggests a decrease in anti-inflammatory factors, which are often associated with tumor progression and immunosuppression(46). This alteration in the macrophage profile further contributes to an environment less favorable for tumor growth and more conducive to effective immune surveillance. These findings suggest that the RIPK3-driven system not only eliminates tumor cells as a safety switch but also reshapes the immune landscape of the TIME, fostering conditions that favor long-term immunity. This reshaping is essential not just for immediate tumor eradication but also for establishing a vigilant immune system capable of responding to future tumor challenges, thereby significantly reducing the risk of recurrence. This aligns with the growing recognition in oncology that the key to effective cancer treatment

lies not only in destroying tumor cells but also in reprogramming the immune system to prevent future occurrences.

TDLNs are the primary sites for the development of adaptive anti-tumor immunity, where activated DCs present tumor-related antigens to CD4+ and CD8+ T cells, leading to cytotoxic T-cell activation and tumor clearance (24). While primary brain tumors in adults rarely metastasize distantly through lymphatic routes, recent research has revealed the existence of meningeal lymphatic vessels connecting the brain to the deep cervical lymph nodes (dCLNs) (47). Although tumor cells themselves may not readily metastasize through these channels, immune cells, antigens, and inflammatory mediators can be transported from the brain to the dCLNs, making them a critical site for studying tumor immunology and potential therapeutic targets. In our study, we focused on the dCLNs as the primary TDLNs, observing an increase in DCs and NK cells post-RIPK3 activation. These findings suggest that RIPK3 activation could potentially enhance the immunogenic capacity of TDLNs, thereby supporting anti-tumor immunity.

While our study focused on the efficacy of the RIPK3-driven necroptotic safety switch using whole living cancer cells which poses more safety concerns than other therapeutic cell types, it is crucial to acknowledge its potential to be implemented in a vast array of cells employed in immunotherapies. Cells such as T cells, NK cells, mesenchymal stem cells, among others, play essential roles in immunotherapeutic strategies. Although the efficacy and safety of the RIPK3 system across these diverse cell types remain unexplored in our study, future research should encompass these cell types to provide a comprehensive understanding of the system's applicability and effectiveness across the spectrum of cell-based immunotherapies.

Moreover, while our study successfully employed immune profiling to discern changes in immune population dynamics, it is important to acknowledge the limitations of this approach. Immune profiling provides a snapshot of the immune landscape, highlighting shifts in cell populations and their potential roles in the immune response. However, this method does not delve into the intricate molecular and cellular mechanisms driving these changes. For instance, while we can observe an increase in the number of mature

DCs in the TME after inducing RIPK3-driven cell death (Fig. 4E), the signaling pathways, transcriptional changes, or intercellular interactions that led to this increase remain elusive. Understanding these underlying mechanisms is crucial, as they can offer insights into the broader implications of our findings, potential therapeutic targets, and the nuances of the immune response. Future studies should aim to bridge this gap, integrating immune profiling with mechanistic investigations or other in-depth analyses to provide a better understanding of the effects observed in cell-based cancer immunotherapy.

In conclusion, our study's introduction of the dual-function RIPK3-driven necroptotic safety switch for cell-based immunotherapies offers a promising avenue to address the safety concerns associated with these therapies as well as synergistically enhance the therapeutic efficacy. By harnessing the immunogenic properties of necroptosis, this system not only ensures safety but also potentially amplifies the therapeutic benefits of cell-based immunotherapies.

Materials and Methods

Sex as a biological variable

Previous studies on both mouse genders have shown consistent results using the same cancer cell-based therapy. Therefore our study focused solely on female mice for easier handling and management purposes.

Study design

The objective of this study was to develop an efficient therapeutic strategy that can simultaneously induce a direct killing of tumor cells and elicit antitumor immune responses to counter the tumor aggressiveness as well as the immunosuppressive microenvironment. We hypothesized that genetic engineering of cancer cells will allow us to use and repurpose their self-homing and neoantigen-rich features for cancer treatment. All experiments performed in this study had at least three replicates to demonstrate biological reproducibility and to ensure adequate statistical power for comparisons. All animals were randomly allocated to the control and treatment groups with equivalent tumor size. The study was not blinded, and no statistical methods were used to predetermine the sample size. Details for *in vivo* experiments, number of cells used, duration, and statistical tests are described below, supplementary materials and figure legends.

Intracranial deep implantation

C57BL6 mice were anesthetized and immobilized on a stereotactic frame. 2 x 10^5 tumor cells in 3µl phosphate-buffered saline (PBS) were implanted 2.2mm deep, 2.5mm lateral from bregma, and 2.5mm ventral from dura in the left hemisphere for the first implantation and in the right hemisphere for the re-challenge. BLI was used to follow *in vivo* growth of Fluc-engineered implanted tumor cells over time using a Perkin-Elmer IVIS Lumina system. For Fluc imaging, mice were imaged 7 min after intraperitoneal injection of D-luciferin (#122799, PerkinElmer). Animals were monitored closely and euthanized at the onset of any humane endpoints, including persistent recumbence, pain or distress that cannot be alleviated by analgesics, difficulty with ambulation, severe central nervous system signs, abnormal breathing and cyanosis, excessive weight loss, tumor production specific endpoints, or model-specific endpoints. Animals were randomly allocated to cages and experimental groups.

Mouse brain tissue and tumor-draining lymph node harvest

C57BL6 mice were perfused with 10ml of PBS by cardiac puncture. Tumor tissues from the brain were then harvested and processed for flow cytometry analysis. To ascertain the brain tumor-draining lymph nodes, we intracranially injected Evans Blue dye and subsequent surgical examination identified the deep cervical lymph nodes as the most proximal TDLNs. Deep cervical lymph nodes were also harvested for flow cytometry analysis.

Cell lines

The mouse GBM cell line CT2A was kindly provided by Dr. I. Verma (Salk Institute). The mouse GBM cell line GL261 was kindly provided by Dr. Sean Lawler (Brown University). All cells were cultured at 37°C in a humidified atmosphere with 5% CO_2 and 1% penicillin/streptomycin (#15140122, Invitrogen) and grown in high glucose Dulbecco's modified Eagle's medium (#11965118, Invitrogen) supplemented with 10% v/v fetal bovine serum (#A4766801, Invitrogen). Cell lines were regularly tested for mycoplasma using a mycoplasma polymerase chain reaction kit (#30-1012K, ATCC).

Determination of B/B, rapamycin, and GCV EC50

The B/B homodimerizer (also called AP20187) was purchased from Sigma Aldrich (#SML2838). A stock solution was obtained by dissolving 5mg of lyophilized B/B in 100% ethanol at a concentration of 62.5mg/mL and stored at -20°C. A working solution was then prepared for serial dilutions of B/B for its EC50 determination, at 100nM, 50nM, 1nM, 0.5nM, 0.25nM and 0.1nM. Rapamycin was purchased from MedChem Express (#HY-10219). Lyophilized rapamycin was dissolved in 6.25% of DMSO in PBS at a concentration of 150mM and stored at 4°C. A working solution was prepared for serial dilutions of rapamycin for its EC50 determination, at 100nM, 50nM, 25nM, 20nM, 15nM, 10nM, 5nM and 1nM. GCV was purchased from Sigma Aldrich (#G2536). Lyophilized GCV was dissolved in 0.1M of HCl at a concentration of 10mg/mL (10 000µg/mL) and stored at -20°C. This solution has been used to perform serial dilutions of GCV for its IEC50 determination, at 50, 25, 10, 5, 2.5, 1, 0.5, and 0.1µg/mL. 1 day before treatment, 10 000 cells per well were plated in 96-well black plates and treated with different doses of B/B

for 3hr, rapamycin for 24hr, or GCV for 72hr. Cell death was observed under the microscope before performing the viability assay. Cells were then rinsed with 50µL of PBS per well before viability was measured using 50µL of 1:50 D-luciferin (#122799, PerkinElmer) in PBS, for Fluc-expressing cells. Bioluminescence was measured using a GloMax® cell plate reader. Experiments were performed in triplicate.

ATP assay

80 000 cells were plated in 24-well plates and treated with EC50 doses of B/B, rapamycin, or GCV at different times to collect samples when about 25%, 50%, and 75% of the cells were dead. The supernatant was collected in microcentrifuge tubes and centrifuged at 9248g for 15minutes at 4°C. The supernatant was then transferred to new centrifuge tubes on ice. A standard curve ATP solution was made from a stock solution at 10mM (#20-306, SigmaAldrich). ATP from ATP standard curve solutions and the ATP within supernatant was then measured using CellTiterGlo® Luminescent Cell Viability Assay kit (#G9241, Promega) diluted at 1:1 in FBS-free medium, and GloMax® cell plate reader in 96-well black plate.

Lentiviral transductions and engineering of stable cell lines

Lentiviral (LV) packaging was performed by transfection of 293T cells using 3rd generation lentiviral systems with calcium chloride. Cells were co-transfected with 12µg of pRRL-EFS-MCS-FV-RIPK3-T2A-GFP lentiviral transfer plasmid and helper DNA (1.2µg of pCMV-VSVG, 2.4µg of pRSV-REV and 3.6µg of pMDLg/pRRE (gag & pol)). After 16hr, the medium was changed to half the original volume of fresh growth medium. 24hr after the medium change, the supernatant was collected without disturbing the cells, centrifuged, and filtered using a 0.45µm PES syringe filter to collect and isolate viruses. Cells were transduced with unconcentrated lentiviral vectors in medium containing protamine sulfate (2µg/mL) in 6-well plates (2 x 10^5 cells per well). After expansion in 100mm tissue culture dishes, CT2A-FmC RIPK3 cells were selected by FACS using a BD FACS Aria Fusion cell sorter. For BLI, cancer cells were transduced with LV-Pico2-Fluc-mCherry and selected by FACS using a BD FACSAria Fusion cell sorter

or puromycin selection (1 μg/ml) in culture. GFP or mCherry expression was confirmed by fluorescence microscopy.

Flow cytometry

Tumor tissues from the brain or deep cervical lymph nodes were collected after perfusion with PBS and subsequently dissociated into single cell suspension through a 100μm cell strainer (#352360, Corning). Cell numbers were counted and resuspended in PBS before staining with viable dye using Zombie UV Fixable Viability Kit (#423107, Biolegend). Next, cells were washed with fluorescence-activated cell sorting (FACS) buffer (2% BSA and 5mM EDTA in PBS) and incubated with mouse FcR blocking reagent (#130-092-575, Miltenyi Biotec) for 30 minutes. Next, the samples were stained with fluorophore-conjugated antibodies (table S3). Antibody dilutions were determined by titration with murine splenocytes. Following staining, samples were washed and fixed with either 2% PFA for extracellular staining or buffers from True-Nuclear Transcription Factor Buffer Set (#424401, Biolegend). Analysis was done using LSR Fortessa Cytometer (BD) with FACSDIVA and FlowJo v10 software using gating strategy as shown in fig. S1. Compensation was done with antibody stained UltraComp eBeads (#01-2222-41, Thermofisher Scientific) and calculated with the FACSDIVA software.

Western blot analysis

After treatment, cells were washed with cold PBS twice, and then lysed with cold RIPA buffer (20 mM Tris-HCl pH 8.0, 137 mM NaCl, 10% glycerol, 1% NP-40, 0.1% SDS, 0.5% Na-deoxycholate, 2 EDTA pH 8.0) supplemented with protease and phosphatase inhibitors (Roche protease inhibitor cocktail; Phosphatase Inhibitor Cocktail I and Phosphatase Inhibitor Cocktail II from Sigma-Aldrich). Cells were then centrifuged at 4°C, 16,000 g for 10 minutes. Supernatant protein concentrations were determined using a Bio-Rad protein assay kit. 6X SDS-sample buffer was added samples, which were then boiled for 3 minutes and resolved on SDS-PAGE gel. 10-40 μg of protein was resolved on SDS-PAGE gel, transferred to nitrocellulose membrane, and probed with primary antibodies. Antibodies against P-MLKL (#37333, Cell Signaling), P-RIPK3 (#91702S, Cell Signaling), caspase3 (#9662S, Cell Signaling), cleaved caspase3

(#9661S, Cell Signaling), HGMB1 (#3935S, Cell Signaling) and anti-Vinculin (#V4505, Sigma-Aldrich) were used for western blotting. HRP-conjugated secondary antibodies against Rabbit (#97023, Abcam) were used for all primary antibodies, except Vinculin for which HRP-conjugated secondary antibodies against mice were used (#97051, Abcam).

TCGA analysis

mRNA expression profile and patient information of tumor samples were extracted from the R2 Genomics Analysis Visualization Platform (https://hgserver1.amc.nl.cgi-bin/r2/main.cgi). Extracted data were entered into Excel and Cluster 3.0 to generate graphs and heatmap. The signature score was calculated by taking the average value of the z score for each gene per sample.

CCGA analysis

mRNA expression profile and patient information of tumor samples were extracted from Chinese Glioma Genome Atlas (http://ccga.org.cn). Extracted data were entered into Excel and Cluster 3.0 to generate graphs and heatmap. The signature score was calculated by taking the average value of the z score for each gene per sample.

Statistical analysis and reproducibility

Data were expressed as mean ±SD for *in vitro* studies and ±SEM for *in vivo* studies and analyzed by Student's t test or 2-Way ANOVA with the two-stage step-up method of Benjamini, Krieger and Yekutieli test for multiple comparison correction. Survival times of mouse groups were analyzed and compared using log-rank (Mantel-Cox) test and Bonferroni correction. GraphPad Prism 9 software was used for all statistical analysis and also to generate Kaplan-Meier survival plots. Differences were considered significant at $P<0.05$ (*), $P<0.01$ (**), $P<0.001$ (***), $P<0.0001$ (****). Experiments were performed with at least three replicates to demonstrate reproducibility and to ensure adequate statistical power for comparisons. The sample sizes for each group for each experiment are shown in figure legends. All mice were randomly assigned to the various experimental groups and all samples were analyzed equally. Exclusion criteria were not preestablished and no sample or data points were omitted from analysis.

Study approval

All *in vivo* procedures were approved by the Institutional Animal Care and Use Committee at Brigham and Women's Hospital.

Data availability

All data are available in the main text or the supplementary materials. All supporting data values are available in the "Supporting data values" XLS file.

References

1. Chen KS, Reinshagen C, Van Schaik TA, Rossignoli F, Borges P, Mendonca NC, et al. Bifunctional cancer cell-based vaccine concomitantly drives direct tumor killing and antitumor immunity. *Sci Transl Med.* 2023;15(677):eabo4778.

2. Li S, Gu C, Gao Y, Amano S, Koizumi S, Tokuyama T, and Namba H. Bystander effect in glioma suicide gene therapy using bone marrow stromal cells. *Stem Cell Res.* 2012;9(3):270-6.

3. Zhou X, Di Stasi A, and Brenner MK. iCaspase 9 Suicide Gene System. *Methods Mol Biol.* 2015;1317:87-105.

4. Griffioen M, van Egmond EH, Kester MG, Willemze R, Falkenburg JH, and Heemskerk MH. Retroviral transfer of human CD20 as a suicide gene for adoptive T-cell therapy. *Haematologica.* 2009;94(9):1316-20.

5. van Schaik TA, Chen KS, and Shah K. Therapy-Induced Tumor Cell Death: Friend or Foe of Immunotherapy? *Front Oncol.* 2021;11:678562.

6. Ahmed A, and Tait SWG. Targeting immunogenic cell death in cancer. *Mol Oncol.* 2020;14(12):2994-3006.

7. Galluzzi L, Buque A, Kepp O, Zitvogel L, and Kroemer G. Immunogenic cell death in cancer and infectious disease. *Nat Rev Immunol.* 2017;17(2):97-111.

8. Fucikova J, Kepp O, Kasikova L, Petroni G, Yamazaki T, Liu P, et al. Detection of immunogenic cell death and its relevance for cancer therapy. *Cell Death Dis.* 2020;11(11):1013.

9. Shibata K, Omahdi Z, and Yamasaki S. Necroptosis DAMPens anti-tumor immunity. *Cell Death Discov.* 2016;2:16033.

10. Tang R, Xu J, Zhang B, Liu J, Liang C, Hua J, et al. Ferroptosis, necroptosis, and pyroptosis in anticancer immunity. *J Hematol Oncol.* 2020;13(1):110.

11. Gong Y, Fan Z, Luo G, Yang C, Huang Q, Fan K, et al. The role of necroptosis in cancer biology and therapy. *Mol Cancer.* 2019;18(1):100.

12. Meng MB, Wang HH, Cui YL, Wu ZQ, Shi YY, Zaorsky NG, et al. Necroptosis in tumorigenesis, activation of anti-tumor immunity, and cancer therapy. *Oncotarget.* 2016;7(35):57391-413.

13. Snyder AG, Hubbard NW, Messmer MN, Kofman SB, Hagan CE, Orozco SL, et al. Intratumoral activation of the necroptotic pathway components RIPK1 and RIPK3 potentiates antitumor immunity. *Sci Immunol.* 2019;4(36).

14. Dhuriya YK, and Sharma D. Necroptosis: a regulated inflammatory mode of cell death. *J Neuroinflammation.* 2018;15(1):199.

15. Raju S, Whalen DM, Mengistu M, Swanson C, Quinn JG, Taylor SS, et al. Kinase domain dimerization drives RIPK3-dependent necroptosis. *Sci Signal.* 2018;11(544).

16. Wu XN, Yang ZH, Wang XK, Zhang Y, Wan H, Song Y, et al. Distinct roles of RIP1-RIP3 hetero- and RIP3-RIP3 homo-interaction in mediating necroptosis. *Cell Death Differ.* 2014;21(11):1709-20.

17. Orozco S, Yatim N, Werner MR, Tran H, Gunja SY, Tait SW, et al. RIPK1 both positively and negatively regulates RIPK3 oligomerization and necroptosis. *Cell Death Differ.* 2014;21(10):1511-21.

18. Chen R, Kang R, and Tang D. The mechanism of HMGB1 secretion and release. *Exp Mol Med.* 2022;54(2):91-102.

19. Zhao Z, Zhang KN, Wang Q, Li G, Zeng F, Zhang Y, et al. Chinese Glioma Genome Atlas (CGGA): A Comprehensive Resource with Functional Genomic Data from Chinese Glioma Patients. *Genomics Proteomics Bioinformatics.* 2021;19(1):1-12.

20. Clackson T, Yang W, Rozamus LW, Hatada M, Amara JF, Rollins CT, et al. Redesigning an FKBP-ligand interface to generate chemical dimerizers with novel specificity. *Proc Natl Acad Sci U S A.* 1998;95(18):10437-42.

21. Khalsa JK, Cheng N, Keegan J, Chaudry A, Driver J, Bi WL, et al. Immune phenotyping of diverse syngeneic murine brain tumors identifies immunologically distinct types. *Nat Commun.* 2020;11(1):3912.

22. Rossignoli F, Hoffman D, Atif E, and Shah K. Developing and characterizing a two-layered safety switch for cell therapies. *Cancer Biol Ther.* 2023;24(1):2232146.

23. Martins I, Wang Y, Michaud M, Ma Y, Sukkurwala AQ, Shen S, et al. Molecular mechanisms of ATP secretion during immunogenic cell death. *Cell Death Differ.* 2014;21(1):79-91.

24. Koukourakis MI, and Giatromanolaki A. Tumor draining lymph nodes, immune response, and radiotherapy: Towards a revisal of therapeutic principles. *Biochim Biophys Acta Rev Cancer.* 2022;1877(3):188704.

25. Power AT, Wang J, Falls TJ, Paterson JM, Parato KA, Lichty BD, et al. Carrier cell-based delivery of an oncolytic virus circumvents antiviral immunity. *Mol Ther.* 2007;15(1):123-30.

26. Raykov Z, Balboni G, Aprahamian M, and Rommelaere J. Carrier cell-mediated delivery of oncolytic parvoviruses for targeting metastases. *Int J Cancer.* 2004;109(5):742-9.

27. Dondossola E, Dobroff AS, Marchio S, Cardo-Vila M, Hosoya H, Libutti SK, et al. Self-targeting of TNF-releasing cancer cells in preclinical models of primary and metastatic tumors. *Proc Natl Acad Sci U S A.* 2016;113(8):2223-8.

28. Garcia-Castro J, Martinez-Palacio J, Lillo R, Garcia-Sanchez F, Alemany R, Madero L, et al. Tumor cells as cellular vehicles to deliver gene therapies to metastatic tumors. *Cancer Gene Ther.* 2005;12(4):341-9.

29. Curry WT, Jr., Gorrepati R, Piesche M, Sasada T, Agarwalla P, Jones PS, et al. Vaccination with Irradiated Autologous Tumor Cells Mixed with Irradiated GM-K562 Cells Stimulates Antitumor Immunity and T Lymphocyte Activation in Patients with Recurrent Malignant Glioma. *Clin Cancer Res.* 2016;22(12):2885-96.

30. Schirrmacher V, Fournier P, and Schlag P. Autologous tumor cell vaccines for post-operative active-specific immunotherapy of colorectal carcinoma: long-term patient survival and mechanism of function. *Expert Rev Vaccines.* 2014;13(1):117-30.

31. Soiffer R, Lynch T, Mihm M, Jung K, Rhuda C, Schmollinger JC, et al. Vaccination with irradiated autologous melanoma cells engineered to secrete human granulocyte-macrophage colony-stimulating factor generates potent antitumor immunity in patients with metastatic melanoma. *Proc Natl Acad Sci U S A.* 1998;95(22):13141-6.

32. Sasso MS, Mitrousis N, Wang Y, Briquez PS, Hauert S, Ishihara J, et al. Lymphangiogenesis-inducing vaccines elicit potent and long-lasting T cell immunity against melanomas. *Sci Adv.* 2021;7(13).

33. Dillman RO, Nayak SK, Barth NM, DeLeon C, Schwartzberg LS, Spitler LE, et al. Clinical experience with autologous tumor cell lines for patient-specific vaccine therapy in metastatic melanoma. *Cancer Biother Radiopharm.* 1998;13(3):165-76.

34. Dillman RO, DeLeon C, Beutel LD, Barth NM, Schwartzberg LS, Spitler LE, et al. Short-term autologous tumor cell lines for the active specific immunotherapy of patients with metastatic melanoma. *Crit Rev Oncol Hematol.* 2001;39(1-2):115-23.

35. Dillman RO, Barth NM, VanderMolen LA, Garfield DH, De Leon C, O'Connor AA, et al. Treatment of kidney cancer with autologous tumor cell vaccines of short-term cell lines derived from renal cell carcinoma. *Cancer Biother Radiopharm.* 2001;16(1):47-54.

36. Dillman RO, Beutel LD, De Leon C, and Nayak SK. Short-term tumor cell lines from breast cancer for use as autologous tumor cell vaccines in the treatment of breast cancer. *Cancer Biother Radiopharm.* 2001;16(3):205-11.

37. Dillman RO, Nayak SK, Brown JV, Mahdavi K, and Beutel LD. The feasibility of using short-term cultures of ovarian cancer cells for use as autologous tumor cell vaccines as adjuvant treatment of advanced ovarian cancer. *Cancer Biother Radiopharm.* 1999;14(6):443-9.

38. Le DT, Picozzi VJ, Ko AH, Wainberg ZA, Kindler H, Wang-Gillam A, et al. Results from a Phase IIb, Randomized, Multicenter Study of GVAX Pancreas and CRS-207 Compared with Chemotherapy in Adults with Previously Treated Metastatic Pancreatic Adenocarcinoma (ECLIPSE Study). *Clin Cancer Res.* 2019;25(18):5493-502.

39. Wu AA, Bever KM, Ho WJ, Fertig EJ, Niu N, Zheng L, et al. A Phase II Study of Allogeneic GM-CSF-Transfected Pancreatic Tumor Vaccine (GVAX) with Ipilimumab as Maintenance Treatment for Metastatic Pancreatic Cancer. *Clin Cancer Res.* 2020;26(19):5129-39.

40. Dillman RO, Cornforth AN, Nistor GI, McClay EF, Amatruda TT, and Depriest C. Randomized phase II trial of autologous dendritic cell vaccines versus autologous tumor cell vaccines in metastatic melanoma: 5-year follow up and additional analyses. *J Immunother Cancer.* 2018;6(1):19.

41. Reinshagen C, Bhere D, Choi SH, Hutten S, Nesterenko I, Wakimoto H, et al. CRISPR-enhanced engineering of therapy-sensitive cancer cells for self-targeting of primary and metastatic tumors. *Sci Transl Med.* 2018;10(449).

42. Davidovich P, Kearney CJ, and Martin SJ. Inflammatory outcomes of apoptosis, necrosis and necroptosis. *Biol Chem.* 2014;395(10):1163-71.

43. Tormoen GW, Crittenden MR, and Gough MJ. Role of the immunosuppressive microenvironment in immunotherapy. *Adv Radiat Oncol.* 2018;3(4):520-6.

44. Tan JK, and O'Neill HC. Maturation requirements for dendritic cells in T cell stimulation leading to tolerance versus immunity. *J Leukoc Biol.* 2005;78(2):319-24.

45. Steinbrink K, Mahnke K, Grabbe S, Enk AH, and Jonuleit H. Myeloid dendritic cell: From sentinel of immunity to key player of peripheral tolerance? *Hum Immunol.* 2009;70(5):289-93.

46. Sumitomo R, Hirai T, Fujita M, Murakami H, Otake Y, and Huang CL. M2 tumor-associated macrophages promote tumor progression in non-small-cell lung cancer. *Exp Ther Med.* 2019;18(6):4490-8.

47. Aspelund A, Antila S, Proulx ST, Karlsen TV, Karaman S, Detmar M, et al. A dural lymphatic vascular system that drains brain interstitial fluid and macromolecules. *J Exp Med.* 2015;212(7):991-9.

Acknowledgments: This work was supported by NIH grants, R01-NS121096 (K.S.). We thank the Department of Education and Research in Biology, ENS Paris-Saclay, Université Paris-Saclay for the support on this project.

Author contributions:

Conceptualization: KS and KSC

Methodology: KSC, SMB, NK, IV, YCC, LYL, FR, PB, SK, NCM, KS

Investigation: KSC, SMB, KS

Visualization: KSC, SMB, KS

Funding acquisition: KS

Project administration: KSC, KS

Supervision: KSC, KS

Writing – original draft: KSC, SMB, KS

Writing – review & editing: KSC, FR, KS

Competing interests:

K.S. owns equity in and is a member of the Board of Directors of AMASA Therapeutics, a company developing stem cell-based therapies for cancer. K.S.'s interests were reviewed and are managed by Brigham and Women's Hospital and Partners HealthCare in accordance with their conflict of interest policies. The other authors declare that they have no competing interests.

Supplementary Materials

Figs. S1 to S5

Tables S1-S3

Figures and Legends

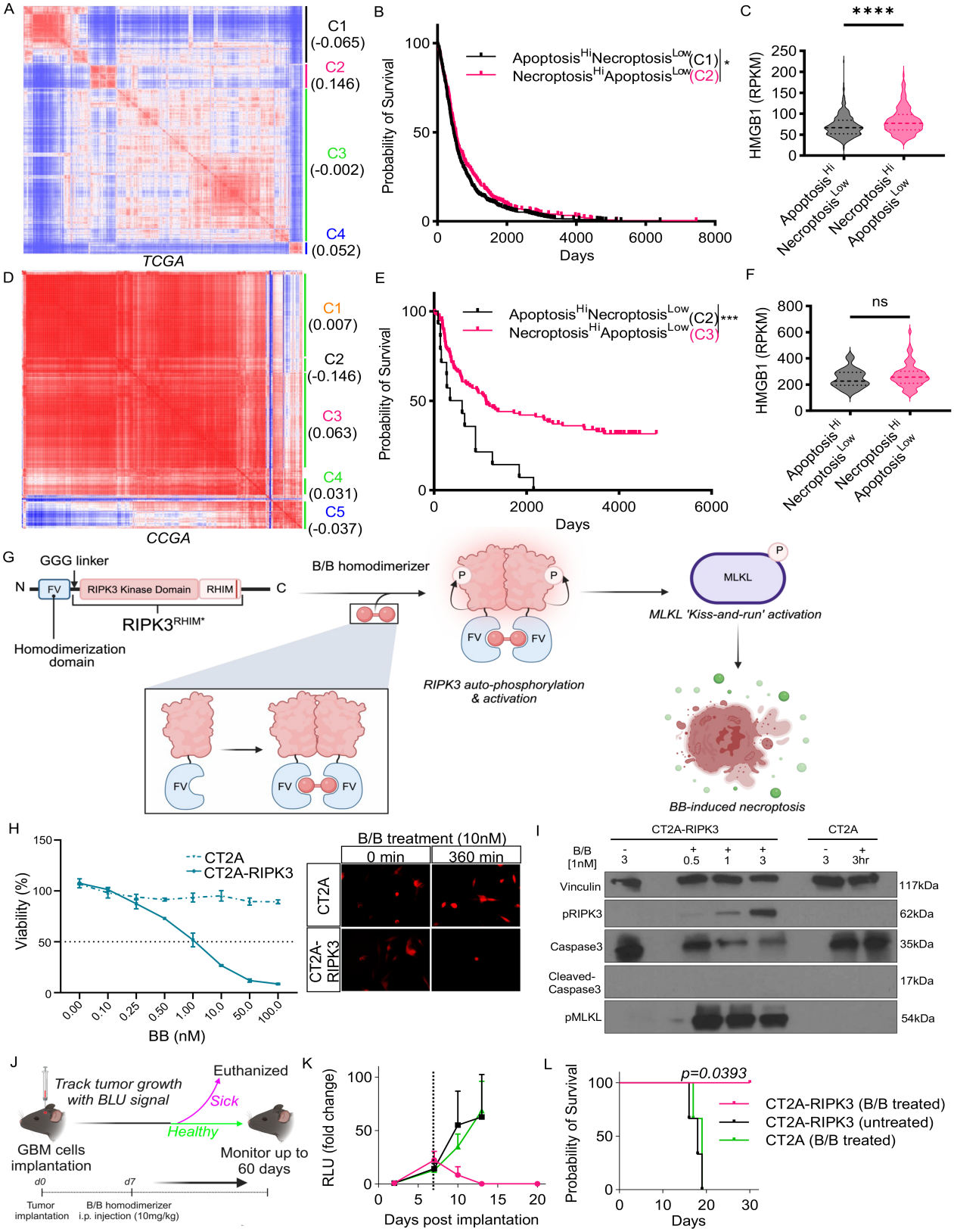

Figure. 1 Establishing an inducible RIPK3-driven necroptotic safety switch. **(A)** Co-clustering of primary tumor samples (*n*=2785) in TCGA based on apoptotic (GO:0097190) and necroptotic (GO:0097527) signaling pathway gene signatures. **(B)** Survival curves by C1 and C2 clusters from (A) for overall survival probability. The survival curves between two groups were compared using log-rank (Mantel-Cox) test and Bonferroni correction. **(C)** Expression of HMGB1 C1 and C2 clusters from (A). **(D)** Co-clustering of primary tumor samples (*n*=222) in CCGA based on apoptotic (GO:0097190) and necroptotic (GO:0097527) signaling pathway gene signatures. **(E)** Survival curves by C2 and C3 clusters from (D) for overall survival probability. The survival curves between two groups were compared using log-rank (Mantel-Cox) test and Bonferroni correction. **(F)** Expression of HMGB1 C2 and C3 clusters from (D). **(G)** Schematic representation of the RIPK3 B/B-inducible safety switch system. **(H)** Cell viability assay of CT2A and CT2A-RIPK3 upon treatment with B/B in a dose-dependent manner for 6 hours and time-lapse imaging of the cells before and after treatment with 10nM of B/B for 6 hours. **(I)** Western blot analysis of pMLKL, pRIPK3, and cleaved-Caspase 3 upon treatment of B/B in CT2A and CT2A-RIPK3 with different durations. **(J)** Schematic of the experimental timeline for intracranial GBM implantation and the treatment schedule for B/B. BLU, bioluminescence. **(K)** Graph of Fluc signal in C57BL6 mice post intracranial implantation with CT2A with B/B treatment (*n*=3), CT2A-RIPK3 with (*n*=3) and without (*n*=3) B/B treatment. Dotted line represents the timepoint of B/B treatment. Bars represent SEM. RLU, relative luminescence unit. **(L)** Kaplan-Meier curves demonstrating the survival probability of the C57BL6 mice post intracranial implantation with CT2A with B/B treatment (*n*=3), CT2A-RIPK3 with (*n*=3) and without (*n*=3) B/B treatment. Log-rank (Mantel-Cox) test and Bonferroni correction.

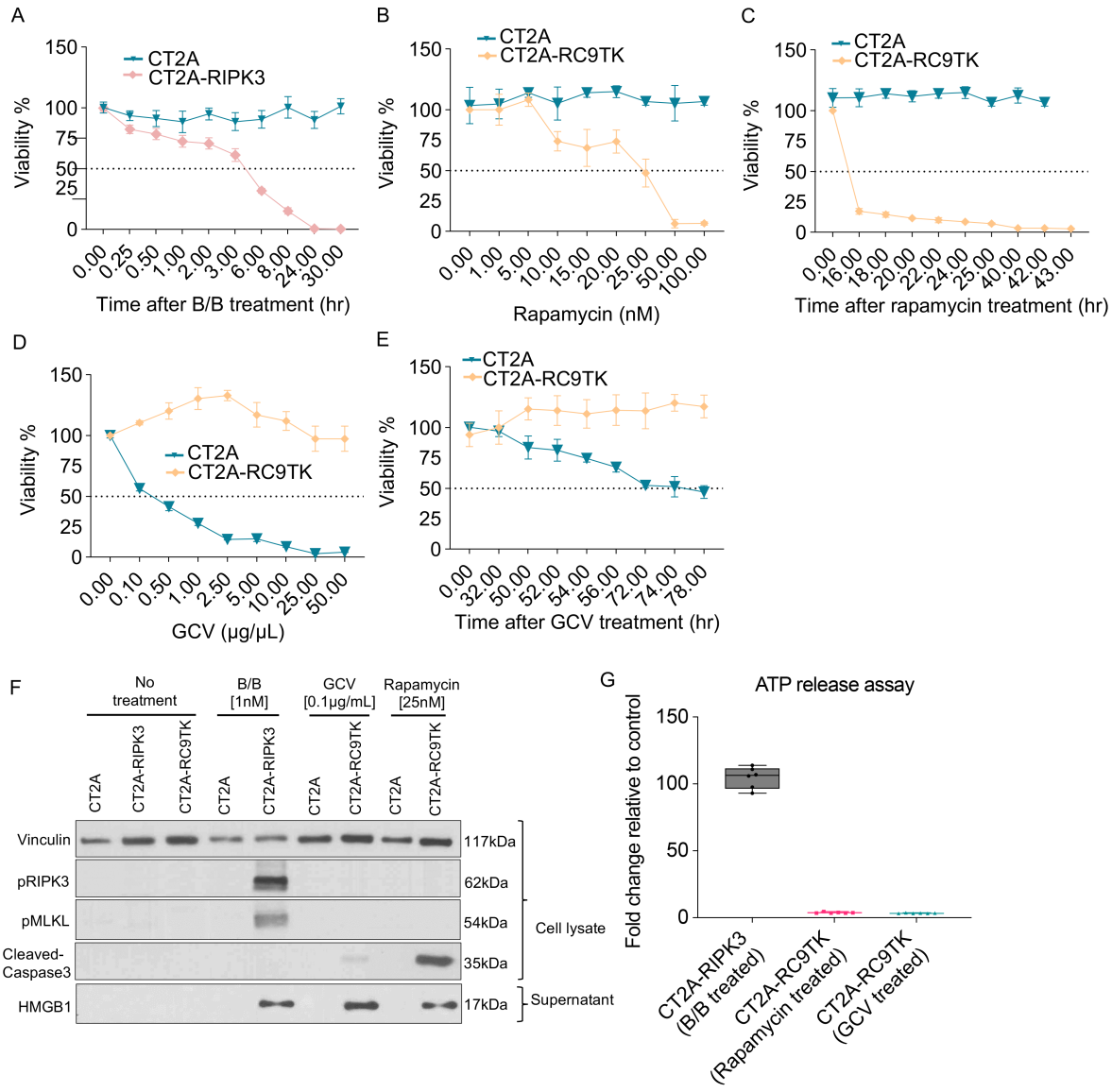

Figure. 2 Cell death induced by RIPK3 safety switch is more immunogenic than RapaCas9 and HSV-TK systems *in vitro*. **(A)** Cell viability assay of CT2A and CT2A-RIPK3 upon treatment with 1nM of B/B in different durations. **(B)** Cell viability assay of CT2A and CT2A-RC9TK upon treatment with rapamycin in a dose-dependent manner for 24 hours. **(C)** Cell viability assay of CT2A and CT2A-RC9TK upon treatment with 25nM of rapamycin in different durations. **(D)** Cell viability assay of CT2A and CT2A-RC9TK upon treatment with GCV in a dose-dependent manner for 72 hours. **(E)** Cell viability assay of CT2A and CT2A-RC9TK upon treatment with 0.1μg/mL of GCV in different durations. **(F)** Western blot analysis of pMLKL, pRIPK3, cleaved-Caspase 3, and HMGB1 upon with or without treatment of B/B in CT2A and CT2A-

RIPK3, with or without treatment of rapamycin or GCV in CT2A and CT2A-RC9TK, based on the respective EC_{50} dose and duration. **(G)** Boxplot of ATP release assay upon with or without treatment of B/B in CT2A and CT2A-RIPK3, with or without treatment of rapamycin or GCV in CT2A and CT2A-RC9TK, based on the respective EC_{50} dose and duration.

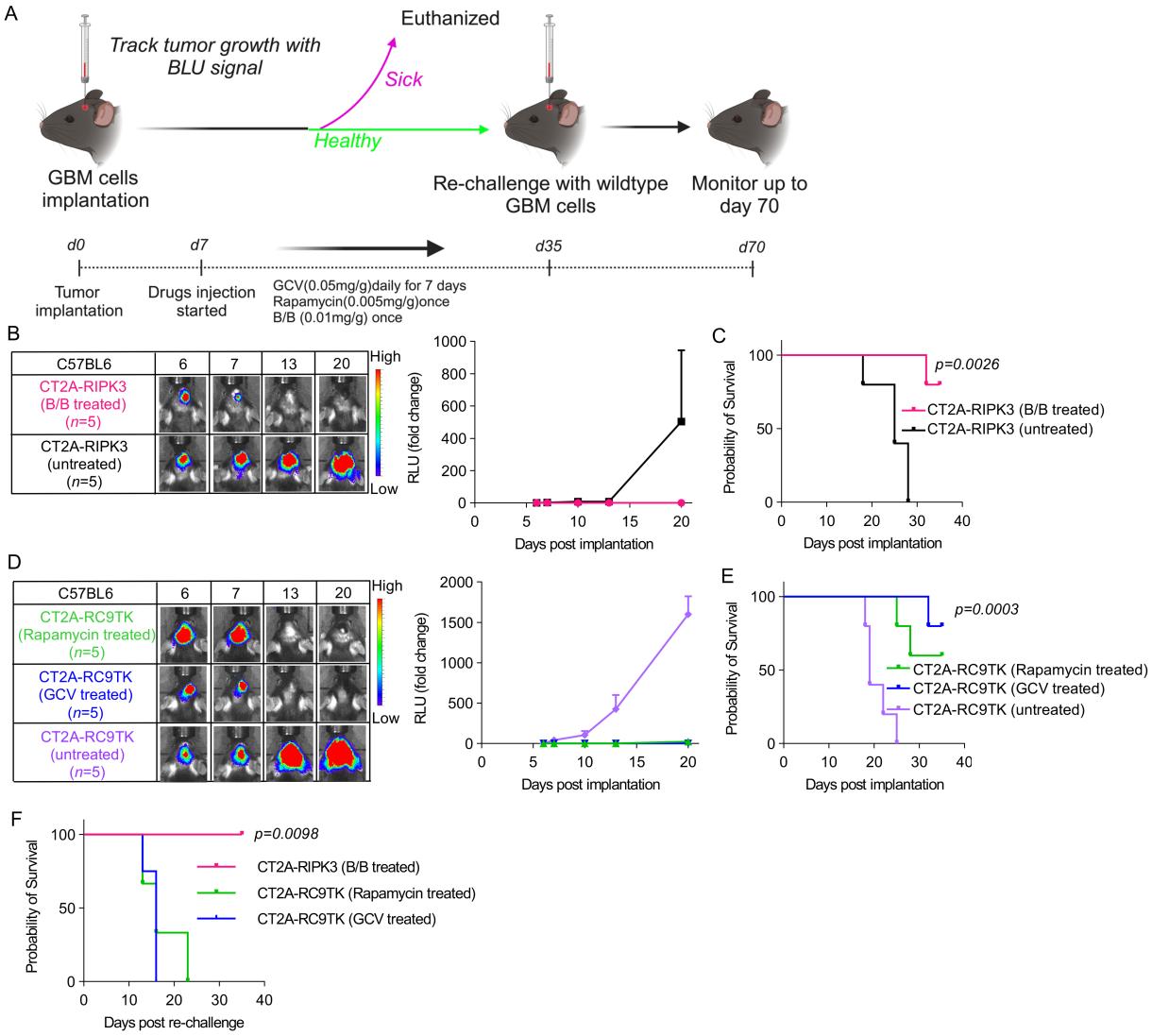

Figure. 3 Tumor cell death induced by RIPK3 safety switch elicits long-term immunity and antitumor therapeutic benefits *in vivo*. **(A)** Schematic of the experimental timeline for intracranial GBM co-implantation and the treatment schedule for B/B, rapamycin, or GCV. BLU, bioluminescence. **(B)** Representative images of Fluc signal (left) and graph of Fluc signal (right) in C57BL6 mice post intracranial

implantation with CT2A-RIPK3 with (*n*=5) and without (*n*=5) B/B treatment. Bars represent SEM. RLU, relative luminescence unit. **(C)** Kaplan-Meier curves demonstrating the survival probability of the C57BL6 mice post intracranial implantation with CT2A-RIPK3 with (*n*=5) and without (*n*=5) B/B treatment. Log-rank (Mantel-Cox) test and Bonferroni correction. **(D)** Representative images of Fluc signal (left) and graph of Fluc signal (right) in C57BL6 mice post intracranial implantation with CT2A-RC9TK with rapamycin treatment (*n*=5), GCV treatment (n=5), and without any treatment (*n*=5). Bars represent SEM. RLU, relative luminescence unit. **(E)** Kaplan-Meier curves demonstrating the survival probability of the C57BL6 mice post intracranial implantation with CT2A-RC9TK with rapamycin treatment (*n*=5), GCV treatment (n=5), and without any treatment (*n*=5). Log-rank (Mantel-Cox) test and Bonferroni correction. **(F)** Kaplan-Meier curves demonstrating survival probability of the surviving C57BL6 mice from (C) and (E) after re-challenge with the parental CT2A cells. Log-rank (Mantel-Cox) test and Bonferroni correction.

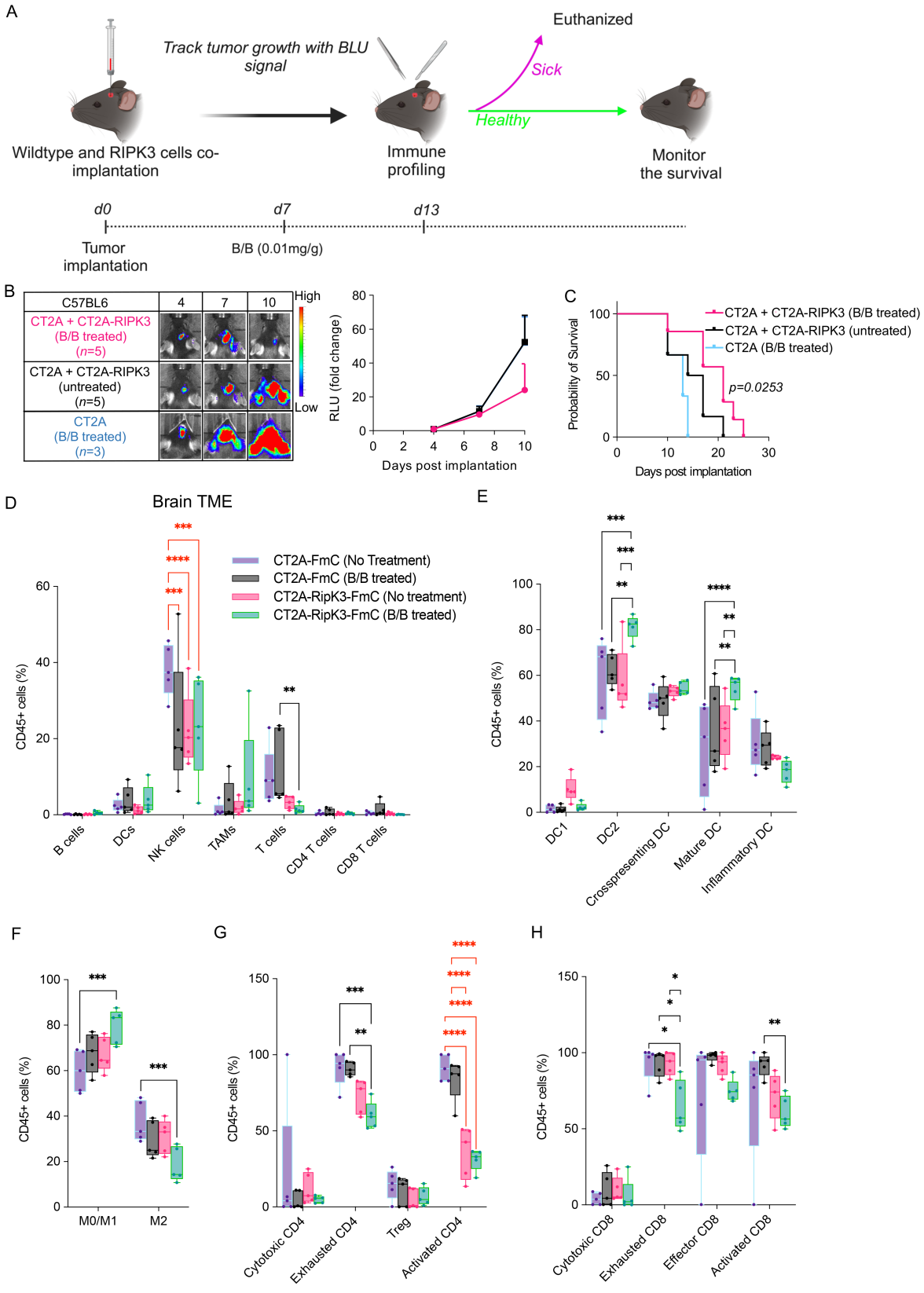

Figure. 4 Cell death induced by RIPK3 safety switch inhibits the tumor growth and reinvigorates tumor immune microenvironment *in vivo*. **(A)** Schematic of the experimental timeline for intracranial mixed GBM

cell implantation and B/B treatment schedule and the tissue collection time for immune profiling. BLU, bioluminescence. **(B)** Representative images of Fluc signal (left) and graph of Fluc signal (right) in C57BL6 mice post intracranial implantation with 150,000 cells of CT2A with B/B treatment (*n*=3), the mixture of 75,000 cells of CT2A and 75,000 cells of CT2A-RIPK3 with (*n*=5) or without (*n*=5) B/B treatment. Bars represent SEM. RLU, relative luminescence unit. **(C)** Kaplan-Meier curves demonstrating the survival probability of the C57BL6 mice post intracranial implantation with CT2A with B/B treatment (*n*=3), the mixture of CT2A and CT2A-RIPK3 with (*n*=5) or without (*n*=5) B/B treatment. Log-rank (Mantel-Cox) test and Bonferroni correction. **(D)** Boxplot showing immune profiling of tumor tissues harvested from the mouse brain 5 days post prodrug treatment for the groups of CT2A with (*n*=5) or without (*n*=5) B/B treatment and the groups of the mixture of CT2A and CT2A-RIPK3 with (*n*=5) or without (*n*=5) B/B treatment. **€** Boxplot showing the profile of DC subpopulations from the experiment in (D). **(F)** Boxplot showing the profile of TAM subpopulations from the experiment in (D). **(G)** Boxplot showing the profile of CD4 T subpopulations from the experiment in (D). **(H)** Boxplot showing the profile of CD8 T subpopulations from the experiment in (D). The whiskers represent minimum to maximum. Data were analyzed by 2-Way ANOVA with the two-stage step-up method of Benjamini, Krieger and Yekutieli test for multiple comparison correction. * = $P<0.05$, ** = $P<0.01$, *** = $P<0.001$, **** = $P<0.0001$. The significance line in black represents changes due to the activation of RIPK3 suicide system, whereas in red represents changes due to differences in cell type or drug.

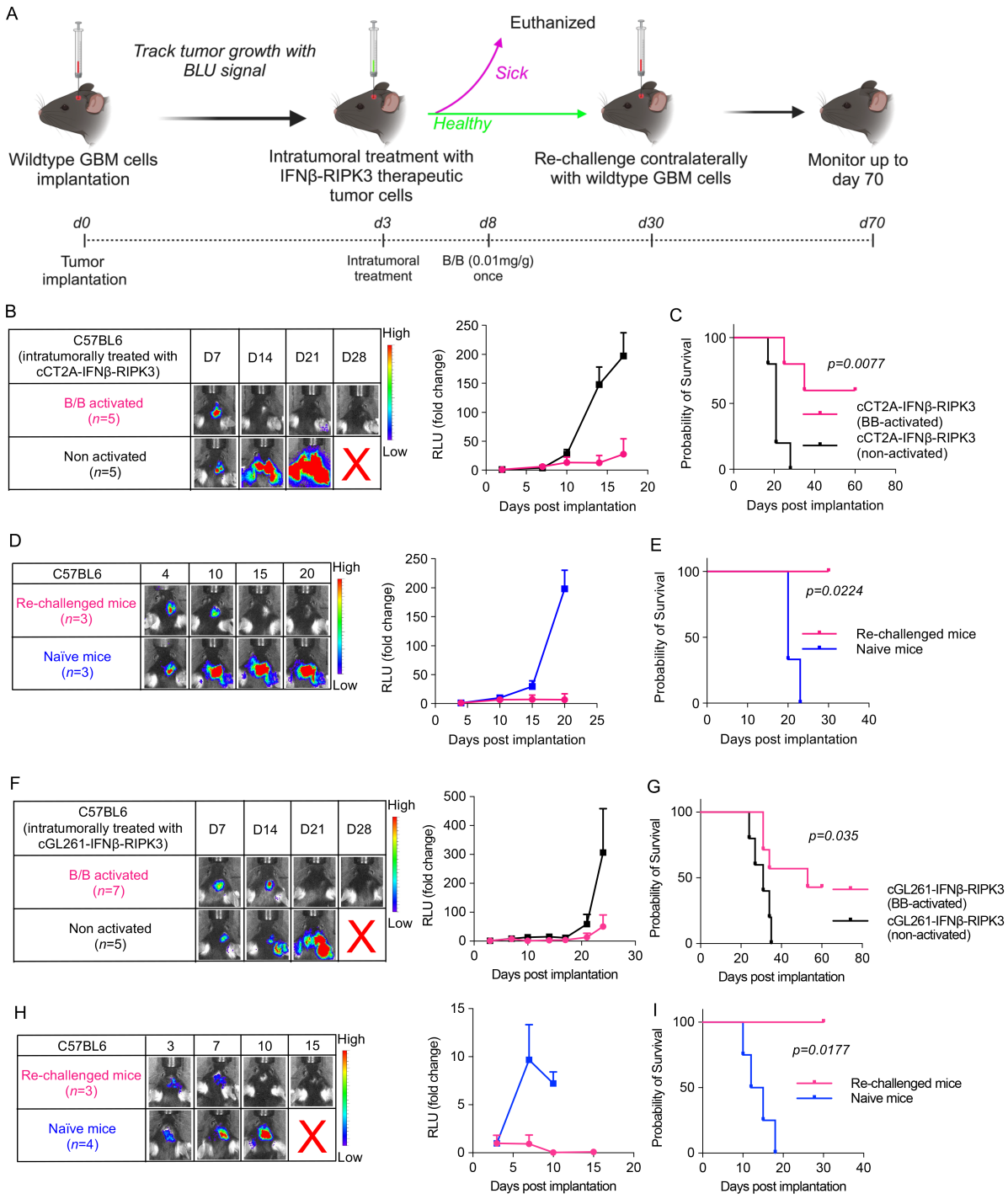

Figure. 5 Tumor cell death induced by RIPK3 safety switch synergistically improves antitumor therapeutic benefits of cancer cell-based therapy and elicits long-term immunity *in vivo*. **(A)** Schematic of the experimental timeline for intracranial GBM implantation, the treatment schedule for cCT2A-IFNβ-RIPK3, and the activation of RIPK3 suicide system via administration of B/B. BLU, bioluminescence. **(B)** Representative images of Fluc signal (left) and graph of Fluc signal (right) in C57BL6 mice post intracranial

implantation of wildtype CT2A and intratumoral treatment with cCT2A-IFNβ-RIPK3 with (*n*=5) or without (*n*=5) B/B administration. Bars represent SEM. RLU, relative luminescence unit. **(C)** Kaplan-Meier curves demonstrating the survival probability of the C57BL6 mice post intracranial implantation of wildtype CT2A and intratumoral treatment with cCT2A-IFNβ-RIPK3 with (*n*=5) or without (*n*=5) B/B administration. Log-rank (Mantel-Cox) test and Bonferroni correction. **(D)** Representative images of Fluc signal (left) and graph of Fluc signal (right) post intracranial implantation with wildtype CT2A in the contralateral brain hemisphere of the surviving C57BL6 mice from (C) (n=3) and naïve mice (n=3). Bars represent SEM. RLU, relative luminescence unit. **(E)** Kaplan-Meier curves demonstrating survival probability of the surviving C57BL6 mice from (C) and naïve mice after re-challenge with wildtype CT2A cells. Log-rank (Mantel-Cox) test and Bonferroni correction. **(F)** Representative images of Fluc signal (left) and graph of Fluc signal (right) in C57BL6 mice post intracranial implantation of wildtype Gl261 and intratumoral treatment with cGL261-IFNβ-RIPK3 with (*n*=7) or without (*n*=5) B/B administration. Bars represent SEM. RLU, relative luminescence unit. **(G)** Kaplan-Meier curves demonstrating the survival probability of the C57BL6 mice post intracranial implantation of wildtype Gl261 and intratumoral treatment with cGL261-IFNβ-RIPK3 with (*n*=7) or without (*n*=5) B/B administration. Log-rank (Mantel-Cox) test and Bonferroni correction. **(H)** Representative images of Fluc signal (left) and graph of Fluc signal (right) post intracranial implantation with wildtype GL261 in the contralateral brain hemisphere of the surviving C57BL6 mice from (G) (n=3) and naïve mice (n=5). Bars represent SEM. RLU, relative luminescence unit. **(I)** Kaplan-Meier curves demonstrating survival probability of the surviving C57BL6 mice from (G) and naïve mice after re-challenge with wildtype GL261 cells. Log-rank (Mantel-Cox) test and Bonferroni correction.